doi:10.2533/chimia.2010.705 Chimia 64 (2010) 705–711

Phase Decomposition upon Alteration of Radiation-Damaged Monazite–(Ce) from Moss, Østfold, Norway

Lutz Nasdala*[a], Katja Ruschel[a], Dieter Rhede[b], Richard Wirth[b], Ljuba Kerschhofer-Wallner[c], Allen K. Kennedy[d], Peter D. Kinny[e], Friedrich Finger[f], and Nora Groschopf[g]

Abstract: The internal textures of crystals of moderately radiation-damaged monazite–(Ce) from Moss, Norway, indicate heavy, secondary chemical alteration. In fact, the cm-sized specimens are no longer mono-mineral monazite but rather a composite consisting of monazite–(Ce) and apatite pervaded by several generations of fractures filled with sulphides and a phase rich in Th, Y, and Si. This composite is virtually a 'pseudomorph' after primary euhedral monazite crystals whose faces are still well preserved. The chemical alteration has resulted in major reworking and decomposition of the primary crystals, with potentially uncontrolled elemental changes, including extensive release of Th from the primary monazite and local redeposition of radionuclides in fracture fillings. This seems to question the general alteration-resistance of orthophosphate phases in a low-temperature, 'wet' environment, and hence their suitability as potential host ceramics for the long-term immobilisation of radioactive waste.

Keywords: Chemical alteration · Monazite–(Ce) · Radiation damage · Thorium silicate

1. Introduction

The accumulation of structural damage generated by the corpuscular self-irradiation of minerals containing actinide elements has been studied widely in the last decades. The bulk radiation damage is caused mainly by alpha-decay events: Recoil of the heavy daughter nuclei upon emission of a ^{4}He core generate nm-sized damage clusters, whose overlapping inter-connection at high densities may lead eventually to the formation of a non-crystalline form.[1,2] Such normally crystalline, irradiation-amorphised minerals are commonly described by the term 'metamict'.[3] The metamictisation process is controlled strongly by the proportion of the rates of damage accumulation and damage annealing; the latter being strongly temperature-dependent.[4,5] Whether or not a certain mineral becomes metamict is consequently not only controlled by the mineral phase itself and the amount of radioactivity it experienced since the time of its growth, but also by its thermal history.

The metamictisation of minerals results in dramatic changes of their physical properties, including volume swelling and potentially subsequent fracturing,[6] a general decrease in elastic properties and hardness,[7] and a change in optical properties[8] (*i.e.* refraction and birefringence). Further, the chemical resistance of metamictised minerals is generally decreased, *i.e.* such materials show enhanced solubility for instance under conditions of near-surface weathering,[9] and enhanced susceptibility to secondary loss of radiogenic isotopes.[10] Knowledge of the self-irradiation behaviour of minerals and their associated property changes are hence of enormous relevance for the Earth sciences (*e.g.* petro-geochemistry and U–Pb geochronology) and the materials sciences (*e.g.* mineral-based matrices for conditioning radionuclides in radioactive waste repositories).[11] In view of the latter, key problems to be studied include i) the susceptibility of materials to undergo chemical alteration, and its increase with cumulative radiation damage, ii) how exactly chemical alteration processes take place, and iii) as to which degree these materials (*i.e.* unaltered and/or altered specimens) can resist the release of radionuclides. The investigation of chemically altered, radiation-damaged minerals is, therefore, motivated strongly by the question, how such materials perform in a low-temperature, 'wet' geological environment over extended periods of time.

2. Material and Methods

2.1 *Sample and Preparation*

We have investigated monazite crystals from a granite pegmatite located at the island of Dillingøya (lake Vannsjø), just east of the city of Moss, Østfold district, south-eastern Norway.[12] The area of origin belongs to the Riphean[13] (which, according to recent timescales of the International Commission of Stratigraphy, corresponds to the Meso- to Neoproterozoic). The monazite crystals are 2–2.5 cm large. They are medium to dark brownish, of thick-tabular habit, and have well-shaped faces with slightly rounded edges.

The monazite crystals were cut through the middle, along their longest dimension, and polished thin sections (~30 μm thickness) attached to a glass slide were prepared. These sections were used for optical microscopy, electron probe micro-analyser (EPMA) investigation, and micro-Raman spectroscopy. Sections were coated with

*Correspondence: Prof. Dr. L. Nasdala[a]
Tel.: +43 1 4277 53220
Fax: +43 1 4277 9532
E-mail: lutz.nasdala@univie.ac.at
[a]Institut für Mineralogie und Kristallographie, Universität Wien
Althanstrasse 14, A–1090 Wien, Austria
[b]Helmholtz-Zentrum Potsdam, Deutsches GeoForschungsZentrum
Telegrafenberg, D–14473 Potsdam, Germany
[c]BWI Informationstechnik GmbH
Balanstr. 73, D–81541 München, Germany
[d]Department of Applied Physics, Curtin University of Technology
Building 301, Kent Street, Bentley, WA 6102, Australia
[e]Department of Applied Geology, Curtin University of Technology
Building 312, Kent Street, Bentley, WA 6102, Australia
[f]Fachbereich Materialforschung und Physik, Universität Salzburg
Hellbrunnerstrasse 34, A–5020 Salzburg, Austria
[g]Institut für Geowissenschaften, Universität Mainz
Johann-Joachim-Becher-Weg 21, D–55099 Mainz, Germany

carbon prior to EPMA imaging and analysis. For Sensitive High mass-Resolution Ion MicroProbe (SHRIMP) analysis, small chips of the sample were, together with the SHRIMP reference MAD–1, embedded in araldite epoxy, and flat polished sample mounts were prepared and coated with gold. For transmission electron microscopy (TEM), electron-transparent foils were prepared by conventional hand-polishing and Ar ion milling at 5 kV. The TEM foils were then coated with carbon.

2.2 *Experimental Details*

The thin sections were first examined and imaged under an optical binocular, in plane-polarised and cross-polarised transmitted light. Raman spectra were obtained in quasi-backscatter geometry using an edge filter-based Renishaw RM1000 system equipped with Leica DMLM optical microscope (50 objective, numerical aperture 0.75) and Peltier-cooled, Si-based charge-coupled device (CCD) detector. Spectra were excited with the 632.8 nm emission of a He–Ne laser. The laser power at the sample surface was ~8 mW, which is well below the threshold for any local sample changes due to intense light absorption. The system was operated in the quasi-confocal mode, resulting in a lateral resolution of ~4–5 μm. Band positions were calibrated using the Rayleigh line and neon lamp emission lines. The wavenumber accuracy was better than 1 cm^{-1}, and the spectral resolution was ~3–4 cm^{-1}.

The chemical composition was determined by means of wavelength-dispersive X-ray spectroscopy (WDS) analysis in a JEOL JXA 8900 RL EPMA. The accelerating voltage was 15 kV and the beam current was 50 nA. The focal spot area of the electron beam had a diameter of <1 μm. Calibration standards used were well-characterized natural and synthetic materials, including YAG (Al, Y), wollastonite (Si), monazite (P), Fe_2O_3 (Fe), $CeAl_2$ (Ce), REE silicate glasses (lanthanides except Ce), crocoite (Pb), Th metals (Th), and UO_2 (U). The CITZAF routine in the JEOL software, which is based on the Φ(ρZ) method,[14] was used for data processing. The results were corrected for rare-earth element (REE) peak overlaps. Back-scattered electron (BSE) imaging, and high-resolution element mapping, were done using a JEOL JXA–8500F thermal field emission-type EPMA. The element distribution maps[15] were obtained in WDS mode with an acceleration voltage of 6 kV, a probe current of 40–50 nA, and a dwell time of 0.25–0.40 s per step (stage step intervals 0.1–0.3 μm).

Transmission electron microscopy – including electron diffraction, bright field (BF) and dark field (DF) imaging, and high-resolution electron microscopy (HREM) imaging – was done using a JEOL 3010 system equipped with LaB6 cathode, and a PHILIPS CM200 system equipped with EDAX X-ray analyser and GATAN imaging filter. The systems were operated at a voltage of 300 kV (JEOL) and 200 kV (PHILIPS), respectively.

Analyses of the U–Th–Pb isotopic composition were done using a SHRIMP II at the Department of Applied Physics, Curtin University of Technology, Perth.[16] The monazite surface was sputtered with a primary, mass-filtered $(O_2)^-$ beam with ~1 nA current, focused to a ~7–10 μm spot. The SHRIMP was operated with a mass resolution (M/ΔM) better than 5000. The sensitivity for Pb isotopes was about 20 counts per second per ppm, per nA. A single analysis consisted of seven scans. Data for each spot were collected in sets of seven scans through the mass range of $^{202}LaPO_2$, $^{203}CePO_2$, ^{204}Pb, background near ^{204}Pb, ^{206}Pb, ^{207}Pb, ^{208}Pb, ^{232}Th, ^{238}U, $^{248}ThO_2$, and $^{270}UO_2$. The total analytical time was *ca.* 16 min per spot. Results were calibrated against MAD–1, a 514 Ma old reference monazite. The ^{204}Pb method was employed for the correction for non-radiogenic Pb.[17,18]

3. Results and Discussion

3.1 *Alteration Textures and Chemical Composition*

Transmitted light and BSE images reveal that the monazite crystals have a remarkably heterogeneous internal texture (Fig. 1). In contrast to the macroscopic appearance of a single-crystal, the material consists of several phases. The specimens are apparent 'pseudomorphs' after primary monazite crystals whose macroscopic crystal shapes are still well-preserved (Fig. 1a), even though they are actually a very heterogeneous composite of phases. The dominant monazite (transparent with pale brownish colour, medium BSE intensity) is inter-grown closely with patches of apatite

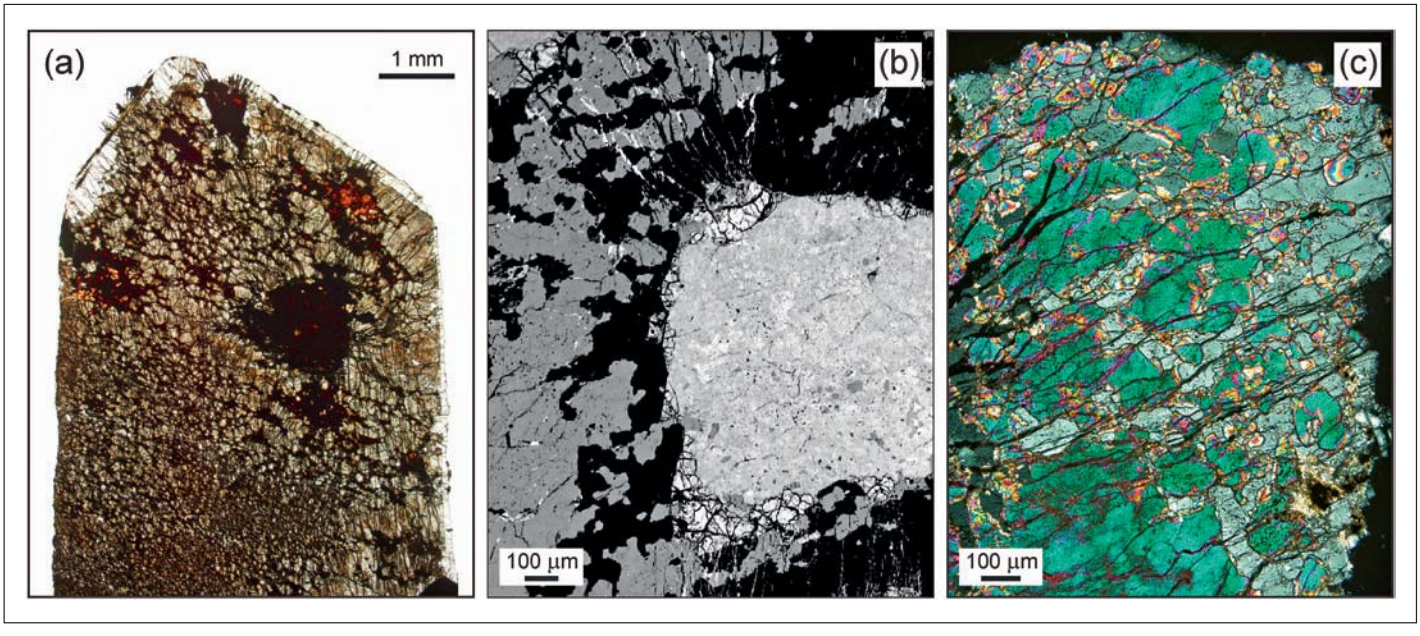

Fig. 1. (a) Photomicrograph of one of the monazite–(Ce) samples (30 μm thin section, transmitted plane-polarised light), revealing its secondary, multi-phase texture. The material is virtually a 'pseudomorph' of a multi-phase composite after a monazite crystal. Note the myriad of fractures emanating from 'nests' consisting of a Th- and Fe-rich material (dark reddish-brown). (b) BSE image, showing one of the 'nests' (centre, bright) that is surrounded by Ca apatite (black; the monazite appears medium gray). (c) Photomicrograph (transmitted cross-polarised light) of the patchy intergrowth of monazite–(Ce) (green interference colour) with apatite (grey interference colour).

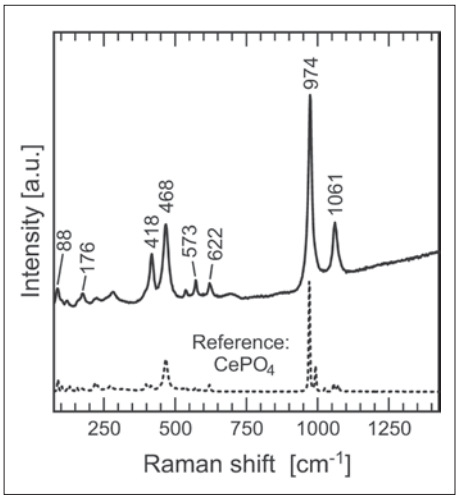

Fig. 2. Raman spectrum of the monazite–(Ce) compared to that of synthetic $CePO_4$.

(colourless, low BSE intensity; Fig. 1a), and a few scattered 'nest'-like patches of a heterogeneous, Th- and Fe-rich material (predominantly hematite; reddish brown, high BSE intensity; Fig. 1b). The phosphate–iron oxide assemblage is pervaded by a network of numerous cracks and fractures up to several tens of μm in thickness, with heterogeneous fracture fillings. The fractures have mostly random orientation but may show a radial pattern around the 'nests', pointing to volume expansion of the Th- and Fe-rich material. In some cases, crystals show a narrow apatite rim (Fig. 1a).

Table 1. Chemical composition of the monazite–(Ce). All values are quoted in wt%.

Oxide	Mean	Range
Al_2O_3	0.0	0.0–0.2
SiO2	1.0	0.7–1.5
P_2O_5	28.8	28.2–29.4
CaO	1.1	0.8–1.7
FeO	0.2	0.0–1.2
Y_2O_3	0.7	0.5–1.0
La_2O_3	8.7	7.6–9.4
Ce_2O_3	25.3	22.4–27.3
Pr_2O_3	3.4	2.9–3.8
Nd_2O_3	12.7	11.2–13.8
Sm_2O_3	6.9	6.3–7.4
Gd_2O_3	3.2	2.8–3.4
Dy_2O_3	0.5	0.2–0.6
Ho_2O_3	0.0	0.0–0.1
PbO	0.4	0.2–1.1
ThO2	6.1	3.7–10.8
UO_2	0.1	0.0–0.3
Σ	99.1	98.3–100.4

In cross-polarised light, the monazite shows high 2nd order to low 3rd order interference colours (Fig. 1c), which corresponds to birefringence in the range 0.028–0.045. The notable but still moderate birefringence depletion, compared to well-crystallised monazite, suggests moderate levels of accumulated radiation damage. The extinction behaviour of the monazite is uniform over large area ranges on the order of millimetres; the same is true for the apatite (*cf.* Fig. 1c). This suggests an oriented (*i.e.* topotaxial) inter-growth of the two phosphate phases.

The mineral phases were identified from their patterns of Raman-active bands. As expected, the vibrational bands of the monazite Raman spectrum correspond to monoclinic $REE[PO_4]$ (*cf.* Fig. 2); however, they show general but still moderate broadening. For instance, the $\nu_1(PO_4)$ band near 974 cm^{-1} has a full width at half maximum (FWHM) of ~13–14 cm^{-1}, which indicates a mildly to moderately radiation-damaged structure.[19] Further mineral phases identified from Raman spectra include fluorapatite $[Ca_5(PO_4)_3F]$, hematite (Fe_2O_3), pyrite (FeS_2), galena (PbS), xenotime (YPO_4), and huttonite ($ThSiO_4$).

The main monazite phase shows a relatively heterogeneous composition (*cf.* ranges quoted in Table 1; *cf.* also BSE image and Fe and Th maps in Fig. 3). The average composition corresponds to the formula $(REE_{0.88}\ Th_{0.05}\ Ca_{0.05}\ Fe_{0.01})\ (P_{0.97}\ Si_{0.04})\ O_4$ (with $REE_{0.88} = Ce_{0.37}\ Nd_{0.18}\ La_{0.13}\ Sm_{0.09}\ Pr_{0.05}\ Gd_{0.04}\ Y_{0.01}\ Dy_{0.01}$). Due to the dominance of Ce at the medium-sized cation position, this mineral is to be called monazite–(Ce). The apatite is relatively homogeneous, pure Ca-phosphate without any non-formula elements in the wt% range. In contrast, the fillings of fractures

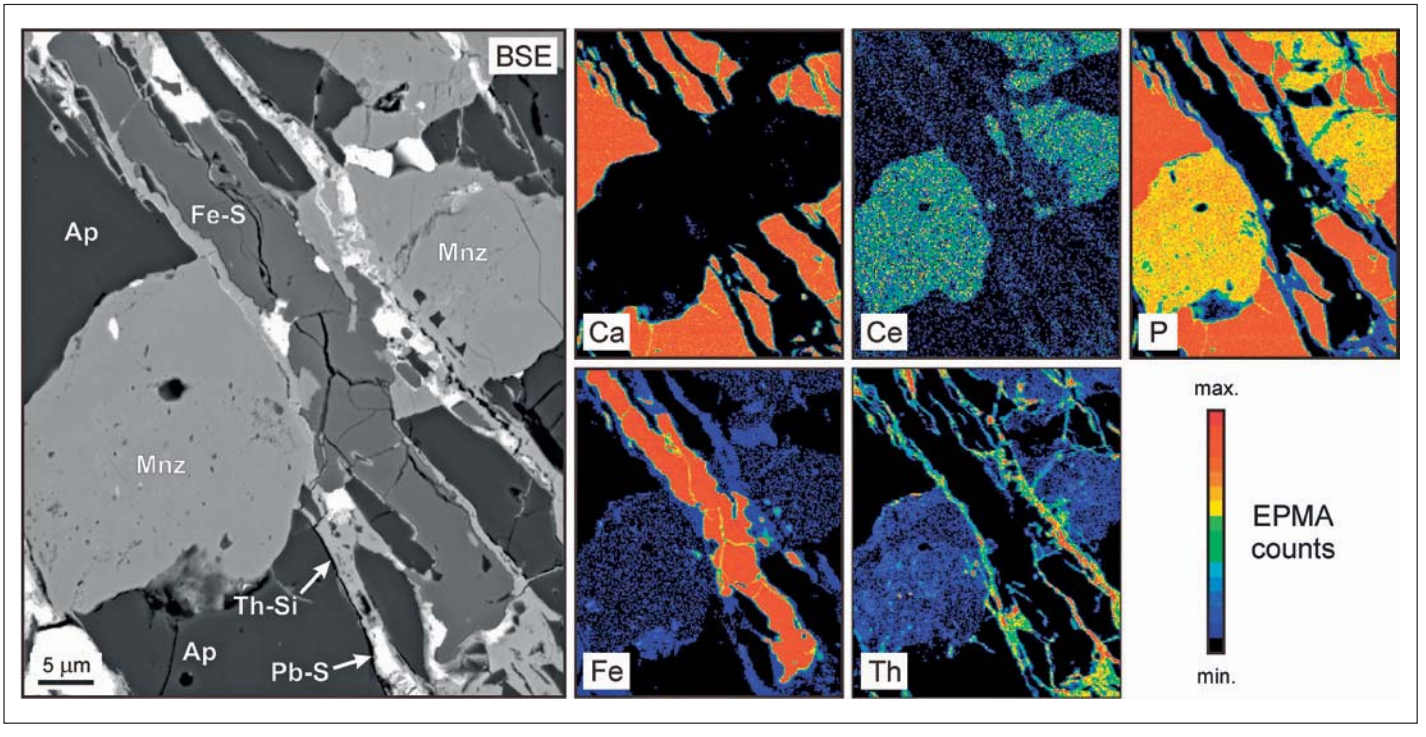

Fig. 3. BSE image, and series of five colour-coded EPMA element distribution maps (6 kV; 4×10^{-8} A; dwell time 0.4 s; step width 0.3 μm) obtained from the same area. In the BSE image, large areas of monazite–(Ce) (Mnz) and apatite (Ap) appear medium gray and nearly black, respectively. These two phosphate phases are inter-grown with veins consisting of Fe sulphide (Fe-S; dark grey), Pb-sulphide (Pb-S; nearly white), and Th-silicate (Th-Si; medium grey). Colour-coded EPMA intensity ranges (given in counts) are 8–339 (Ca), 1–16 (Ce), 12–516 (P), 63–1919 (Fe), 4–142 (Th).

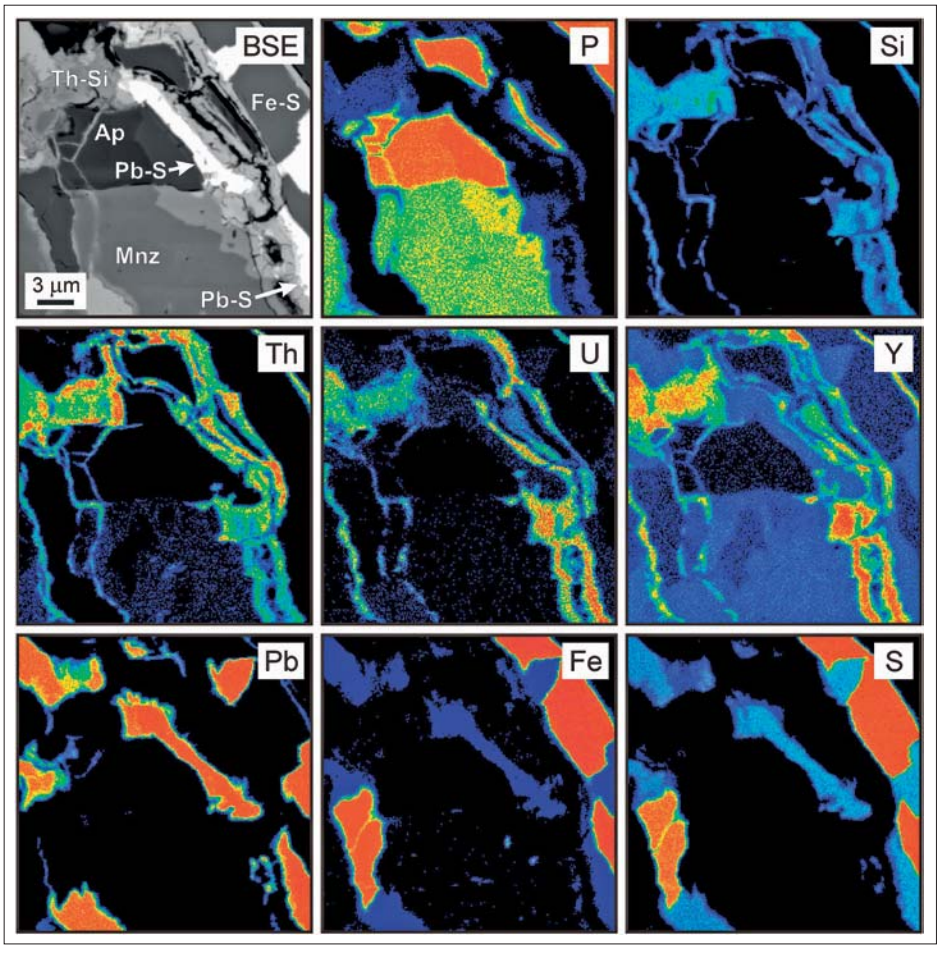

Fig. 4. BSE image showing a close-up of veins cross-cutting the two bulk phosphates, and corresponding series of eight colour-coded element distribution maps (6 kV; 5×10^{-8} A; dwell time 0.4 s; step width 0.1 µm). Colour-coded EPMA intensity ranges (given in counts) are 10–465 (P), 3–199 (Si), 5–168 (Th), 2–59 (U), 15–243 (Y), 13–592 (Pb), 83–1758 (Fe), 16–542 (S).

pervading the two bulk phosphates are most heterogeneous in composition (Fig. 3). Apparently there are several 'generations' of veinlets. The central fillings are dominated typically by Fe-sulphide (*i.e.* pyrite) whereas towards the rims of fractures there is Pb-sulphide (*i.e.* galena; bright BSE) associated with a Th-rich phase (*cf.* Fe and Th distribution maps in Fig. 3).

The distribution patterns of several elements discussed are shown at higher resolution in Fig. 4. In fractures there are large pyrite (red in the Fe and S maps) and galena grains (red in the Pb and pale blue in the S map). The Th-rich phase, which seems to be the youngest, may occupy much smaller fractures. Phosphorous and the REEs are depleted appreciably in these Th-rich veinlets, compared to the bulk monazite–(Ce) (Fig. 3). Apart from a clear enrichment in Th (which may exceed 50 wt% in single spots) and Si, there is also an enrichment in Fe, Y, and U. However, element ratios are non-uniform (note the clear differences between the Th map on the one hand and the U and Y maps on the other hand in Fig. 4). Obviously the Th-rich veinlets do not represent one mineral phase but consist of a heterogeneous assemblage of several phases with different compositions.

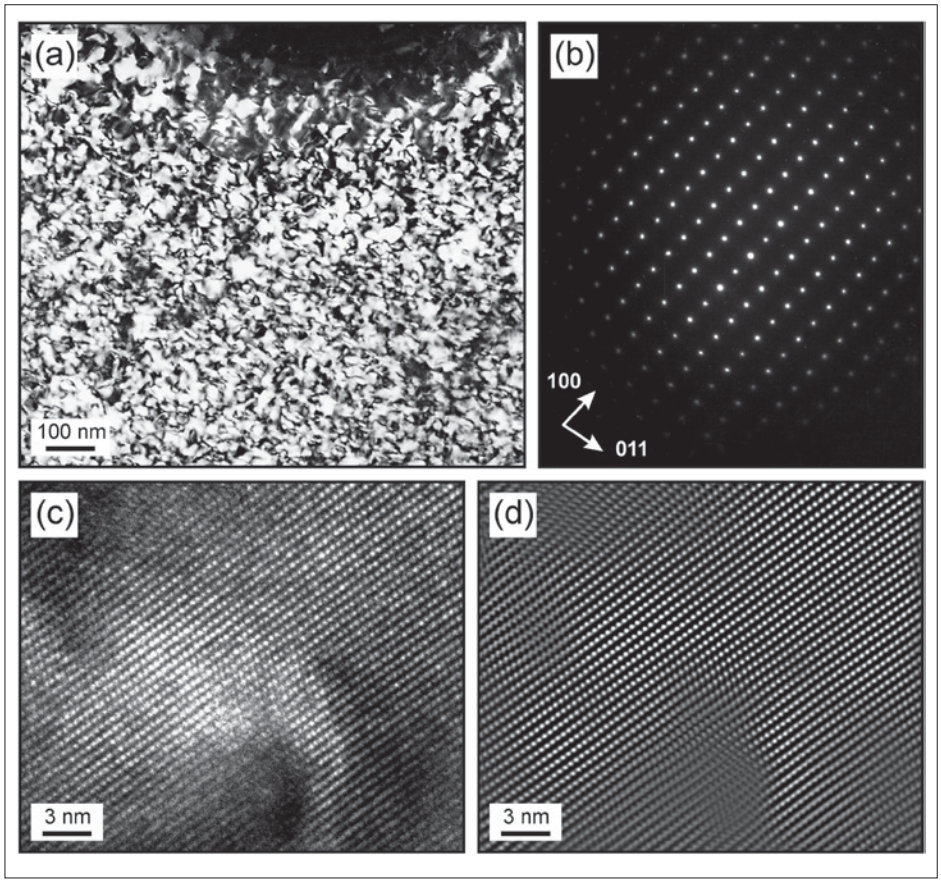

Fig. 5. TEM results for the bulk monazite. (a) Dark field image (diffracting vector g = 311) showing mottled contrast. (b) Electron diffraction pattern obtained along [0$\bar{1}$1]. (c) HREM lattice fringe image (viewed along [010]). (d) Fourier-filtered version of the same image. Note the absence of aperiodic regions.

3.2 *Transmission Electron Microscopy*

Dark-field images of the monazite show mottled contrast (Fig. 5a), which is assigned to a mosaic-like domain texture (*i.e.* volume regions with slightly varying orientation) resulting from self-irradiation damage.[19,20] The degree of misorientation and the volume fraction of distorted regions in our sample are not extensive, because sharp maxima were observed in the electron diffraction patterns (Fig. 5b). The domain texture is also recognised in high-resolution lattice-fringe images (Figs. 5c–d) showing well-ordered, periodic lattice regions up to a few tens of nanometres in size, bracketed by slightly confused boundary regions. These observations suggest that the monazite represents a moderate degree of accumulated self-irradiation damage,[21] which also corresponds well with the still high interference colours (Fig. 1c) and the moderate broadening of Raman bands (Fig. 2).

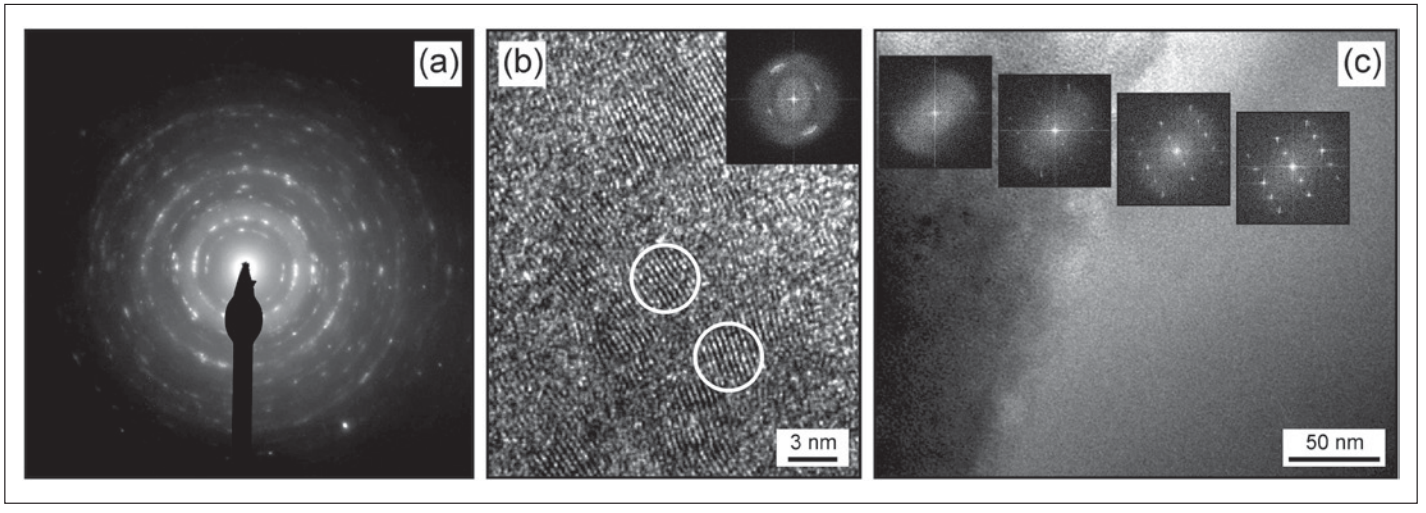

Fig. 6. TEM results (continued). (a) Electron diffraction pattern of a Th-rich veinlet, indicating the polycrystalline nature of the material. (b) HREM image of the Th-silicate phase. Two of the nanometre-sized 'crystalline islands' having different orientation are marked with white circles. The corresponding FFT electron-diffraction pattern (inset) shows strongly broadened maxima. (c) Bright-field image of the apatite in close proximity to a Th-silicate vein (located on the left, just outside the image area). The positions of the four insets correspond roughly to the locations where the FFT electron-diffraction patterns were obtained. Note the gradual loss of apatite crystallinity toward the Th-silicate.

The Th-rich phase, occurring as outer fracture filling in the veinlets (*cf.* BSE image and Th map in Fig. 3), shows a more diverse appearance in the TEM. Electron diffraction patterns obtained from sample volumes of more than a few nanometres in size are characterized by coarse rings of broadened diffraction maxima, which are overlaid by an always notable, diffuse 'amorphous ring' (Fig. 6a). This suggests that the Th-rich material is partially amorphous and partially crystalline, hence probably containing several phases. The crystalline volume fraction must be polycrystalline, consisting of a multitude of tiny crystals (or better, ordered volume regions) with slightly different orientations. The rotation of the crystalline volume regions can be observed in high-resolution lattice-fringe images (Fig. 6b); this phenomenon is due to local strain as induced by the amorphisation.[2]

In high-resolution electron-diffraction patterns of the Th-rich material, generated through fast Fourier-transformation (FFT) of HREM images, diffraction maxima show in some cases clear broadening (for instance, *cf.* inset in Fig. 6b). The d-spacings calculated from FFT electron-diffraction patterns point to a decidedly heterogeneous material. A set of d-values of ~0.47 and ~0.36 nm may be assigned to the (101) and (200) of zircon-structured $ThSiO_4$ (*i.e.* thorite), whereas ~0.42, ~0.33, ~0.31, and ~0.29 nm correspond to the ($\bar{1}$11), (200), (120), and (012) of monazite-structured $ThSiO_4$ (*i.e.* huttonite). A set of d-values of ~0.33 and ~0.28 nm may perhaps even indicate the additional presence of cubic ThO_2 (*i.e.* thoriantite), as they correspond reasonably well with the (111) and (200) of this mineral; there is, however, some potential overlap with huttonite (*cf.* above). These observations suggest a moderate to high level of accumulated radiation damage in the Th-silicate veinlets, which has, however, remained well below the level of complete amorphisation. The notably heterogeneous phase composition of the Th-rich veinlets seems to agree well with their chemical heterogeneity discussed above and may point to a non-homogeneous (*i.e.* multi-step) formation process of the veinlet material.

An interesting observation was made for the Ca apatite. The bulk of this phase is in the crystalline state, without mottled contrast in BF images or any other indication of low levels of radiation damage. The situation is different, however, in the case of apatite that is located in close proximity to Th-rich veinlets (*i.e.* up to ~150 nm away from the veinlet–apatite boundary). Toward the Th-rich veinlets, the apatite is increasingly damaged, up to complete amorphisation (Fig. 6c). The damaged/amorphised zone is interpreted as alpha-recoil halo,[22,23] *i.e.* the damage in the apatite was generated mainly by recoils of heavy nuclei originating from the high Th content in the neighbouring veinlet material.

3.3 *Geo-Chronological Considerations*

An attempt was made to determine the age of the monazite–(Ce) formation and/or the time of its alteration using SHRIMP U–Th–Pb measurements. However, the material turned out to be virtually 'undatable': Even though all measurements were placed carefully in apparently crack-free material, the isotope ratios obtained show extensive scatter and are tainted with huge uncertainties, resulting in calculated $^{207}Pb/^{206}Pb$ ages for single measurements with 2σ errors as high as several hundred Ma (average 1027±221 Ma; Table 2). This may first be due to the hypothetical presence of scattered, sub-micrometre sized Pb-rich domains in radiation-damaged monazite.[24] Most importantly, our monazite–(Ce) sample contains varying but generally very high concentrations of common Pb (*cf.* f 206 values in Table 2), resulting in very large ^{204}Pb corrections to the isotopic ratios and hence increased uncertainties. In addition to the introduction of common Pb, the U–Th–Pb isotopic system also seems to be affected by secondary loss of the radiogenic Pb. This is indicated by significantly discordant isotope ratios (Table 2).

Following the method of Montel *et al.*,[25] we attempted also to calculate monazite U–Th–Pb ages from EPMA results. Measurements in carefully selected, apparently unaltered areas of the monazite–(Ce) yielded an average 'age' of 788±34 Ma (2σ).

Both of the above two age values are uncertain, and none of them is considered to be a realistic age, because of the isotopic ratios being biased notably by the disturbance of the U–Th–Pb system (in particular Pb loss and Pb gain) during the alteration. The high fraction of common Pb indicates that significant amounts of Pb were incorporated during the alteration. This conclusion agrees very well with elevated concentrations of Pb (partly occurring as PbS) in the secondary fracture fillings (*cf.* Pb and S maps in Fig. 4), which has been observed similarly by Poitrasson *et al.*[26] Even in view of the uncertainties, the U–Th–Pb elemental and isotopic ratios obtained point to a Proterozoic (*i.e.* Meso- to Neoproterozoic) age. It could either be assigned to the primary pegmatitic growth

Table 2. SHRIMP data for the monazite–(Ce) from Moss, Norway. All errors represent 2σ uncertainties

(a) Measured isotope ratios (not corrected for common Pb):

Spot	$^{204}Pb/^{206}Pb$	$^{207}Pb/^{206}Pb$	$^{208}Pb/^{206}Pb$	$^{206}Pb/^{238}U$	$^{207}Pb/^{235}U$
1	0.00691±0.00080	0.172±0.004	106.0±1.1	0.175±0.053	4.17±1.28
2	0.00429±0.00031	0.125±0.001	71.3±0.4	0.0827±0.0013	1.419±0.029
3	0.0176±0.0007	0.328±0.006	44.6±0.6	1.076±0.034	48.7±1.9
4	0.00250±0.00017	0.114±0.001	23.9±0.1	0.192±0.003	3.00±0.05

(b) Data corrected for common Pb (^{204}Pb method):

Spot	f 206[a] [%]	$^{206}Pb/^{238}U$	$^{206}Pb/^{236}U$ age [Ma]	$^{207}Pb/^{235}U$	$^{207}Pb/^{235}U$ age [Ma]	$^{207}Pb/^{206}Pb$	$^{207}Pb/^{206}Pb$ age [Ma]	Disc.[b] [%]
1	11.0	0.156±0.047	934±262	1.61±0.61	973±243	0.075±0.015	1065±404	12
2	6.8	0.0770±0.0012	478±7	0.667±0.059	519±36	0.0629±0.0053	704±180	32
3	28.2	0.773±0.027	3691±99	8.48±1.95	2282±212	0.080±0.018	1187±453	–211
4	4.0	0.184±0.003	1088±14	1.98±0.09	1108±29	0.0782±0.0030	1151±77	5

[a]f 206 = common ^{206}Pb / total ^{206}Pb, from the observed ^{204}Pb
[b]U–Pb discordance; ratio of the ^{204}Pb-corrected $^{206}Pb/^{238}U$ and $^{207}Pb/^{206}Pb$ ages

of the monazite–(Ce) [this interpretation is supported by the monazite's chemical composition (relatively high concentrations of intermediate REEs) and EPMA totals of close to 100 wt% (Table 1)[27]] or be interpreted as a metasomatic overprint age (supported by the high common Pb).

Assuming a ~1000 myr damage accumulation period for the host monazite–(Ce), and based on its Th and U concentrations (Table 1), an average time-integrated alpha fluence[5,28] of $\sim 4.5 \times 10^{19}$ g^{-1} is calculated. Even in view of the strong uncertainty of the age that was used to calculate this fluence, the value calculated surpasses appreciably the alpha dose of $<1 \times 10^{19}$ α/g^{-1} that is needed for the complete amorphisation of solids.[2] Consequently, if all of the alpha-event damage experienced over a ~1000 myr time period was stored, our sample should be amorphous. By contrast, the bulk monazite–(Ce) is found to be only mildly to moderately radiation-damaged, hence obviously representing a comparably low degree of damage accumulation. This observation indicates extensive thermal annealing experienced by the Moss monazite (which in turn is completely consistent with the general observation that natural monazite, which undergoes thermal annealing at comparably low temperatures, virtually never becomes fully metamict[19,24]).

4. Concluding Remarks

The partial replacement of monazite by secondary apatite is commonly observed,[29] however, the opposite situation, *i.e.* secondary monazite occurring within apatite, is also a well-known phenomenon.[30,31] A rather special case was reported by Seydoux-Guillaume *et al.*[32] and Hetherington and Harlov[33] who found Th-rich monazite to have decomposed into Th-poor monazite and Th-silicate, without the presence of any apatite, however with alteration textures largely similar to those observed in this present study. It has been observed more often that a secondary Th–Si phase (or, more correctly, a heterogeneous phase assemblage rich in Th and Si) is formed upon decomposition of monazite to form apatite.[25,34,35] In such cases, the secondary apatite occurs mostly as microscopic, fine-grained overgrowth rim or interspace filling, with the Th-rich phase being located in close proximity. Our sample seems to be analogous, however, with an unusually high degree of phase separation: The apatite is crystallographically homogeneous on a comparably large scale (Fig. 1c), indicating a close topotactic relationship[30,36] with monazite, and it occurs relatively well separated from the Th–Si phase, which is located in fractures. The occurrence of a significant volume fraction of apatite within the monazite–(Ce) suggests that the alteration fluid was rich in F.

As early as one century ago, it has been discussed that a notable portion of the radioactivity in monazite from Moss, Norway, may arise from included Th-silicate.[37] However, it was also found that the excess Th cannot, at least not solely, be present in the form of $ThSiO_4$, because of variable, and mostly too low, Si/Th ratios.[38] Our observations support the presence of a heterogeneous secondary phase rich in Th and Si, and characterise the 'monazite crystals' from Moss as poly-phase 'pseudomorphs' with a complex chemical and thermal post-growth alteration history. In view of sharp boundaries and the extremely low volume diffusion of Th in monazite,[39] the alteration is assigned to a fluid-driven dissolution and 'pseudomorphisation' process[40] which released the Th into the alteration fluid. This was followed by re-deposition in the form of Th-rich phases (however, these phases grew obviously only after the formation of Fe- and Pb-sulphides in the fractures). The clear textural separation of Th-free Ca-apatite and Th-rich fracture fillings observed may indicate a multi-step alteration involving secondary Th depletion and tertiary Th enrichment (the latter being connected with the incorporation of common Pb).

Our observations reconfirm that under conditions of fluid-driven alteration and/or low-grade metamorphism, monazite may undergo very complex chemical alteration. The susceptibility to such alteration (and hence the probability for the release of radionuclides) does not only depend on the alteration fluid[25] but may be enhanced potentially by the accumulation of self-irradiation damage. It has been discussed by Read *et al.*[35] that this may have important implications for the chemically similar Pu^{4+}, questioning the suitability of monazite-structured orthophosphates as ceramics for the long-term immobilisation of radionuclides under the potentially 'wet', low-temperature conditions of waste repositories.

Acknowledgements

The sample was kindly made available by A. Massanek from the mineral collection of TU Bergakademie Freiberg, Germany. We are most grateful to D. Dettmar (Bochum), K. Paech (Potsdam), and A. Wagner (Wien) for sample preparation. Thanks are due to H.-J. Berg and F. Corfu (Oslo) for literature advice and helpful comments on the occurrence of monazite in southern Norway, and to A.-M. Seydoux-Guillaume for fruitful discussions

on problems related to monazite alteration. The manuscript benefited from constructive comments by I. Broska and P. Uher (Bratislava), K. Mezger (Bern), and an anonymous expert. L.N. is indebted to W. Hofmeister (Mainz) and W. Heinrich (Potsdam) for financial support during the early stages of this research. Partial funding was provided by the German Research Council (DFG), grant Na284/2–1, the European Commission trough contract no. MEXC–CT–2005–024878, and the Austrian Science Fund (FWF), grants P20028–N10 to L.N. and P22408 to F.F.

Received: July 30, 2010

[1] a) P. J. Wasiliewski, F. E. Senftle, J. E. Vaz, A. N. Thorpe, C. C. Alexander, *Rad. Effects.* **1973**, *17*, 191; b) W. J. Weber, R. C. Ewing, C. R. A. Catlow, T. D. de la Rubia, L. W. Hobbs, C. Kinoshita, H. Matzke, A. T. Motta, M. Nastasi, E. K. H. Salje, E. R. Vance, S. J. Zinkle, *J. Mater. Res.* **1998**, *13*, 1434; c) S. X. Wang, L. M. Wang, R. C. Ewing, *Phys. Rev. B* **2001**, *63*, 41051; d) R. C. Ewing, W. J. Weber, J. Lian, *J. Appl. Phys.* **2004**, *95*, 5949, and references therein.

[2] W. J. Weber, R. C. Ewing, L.-M. Wang, *J. Mater. Res.* **1994**, *9*, 688.

[3] a) W. C. Brøgger, *Z. Kryst. Mineral.* **1895**, *25*, 427; b) R. C. Ewing, *Nucl. Instrum. Meth. B* **1994**, *91*, 22; c) E. K. H. Salje, J. Chrosch, R. C. Ewing, *Am. Mineral.* **1999**, *84*, 1107.

[4] a) A. Meldrum, L. A. Boatner, R. C. Ewing, *Phys. Rev. B* **1997**, *56*, 13805; A. Meldrum, L. A. Boatner, R. C. Ewing, *Miner. Mag.* **2000**, *64*, 183; c) L. Nasdala, P. W. Reiners, J. I. Garver, A. K. Kennedy, R. A. Stern, E. Balan, R. Wirth, *Am. Mineral.* **2004**, *89*, 219.

[5] L. Nasdala, M. Wenzel, G. Vavra, G. Irmer, T. Wenzel, B. Kober, *Contrib. Mineral. Petrol.* **2001**, *141*, 125.

[6] a) L. W. Hobbs, F. W. Clinard, S. J. Zinkle, R. C. Ewing, *J. Nucl. Mater.* **1994**, *216*, 291; b) J. K. W. Lee, J. Tromp, *J. Geophys. Res.* **1995**, *100*, 17753.

[7] a) H. Özkan, *J. Appl. Phys.* **1976**, *47*, 4772; b) B. C. Chakoumakos, W. C. Olivier, G. R. Lumpkin, R. C. Ewing, *Radiat. Eff. Defect. S.* **1991**, *118*, 393; c) W. C. Olivier, J. C. McCallum, B. C. Chakoumakos, L. A. Boatner, *Radiat. Eff. Defect. S.* **1994**, *132*, 131.

[8] B. C. Chakoumakos, T. Murakami, G. R. Lumpkin, R. C. Ewing, *Science* **1987**, *236*, 1556.

[9] a) R. C. Ewing, R. F. Haaker, W. Lutze, in 'Scientific basis for radioactive waste management, 5', Ed. W. Lutze, Elsevier, Amsterdam, **1982**, p. 389; b) E. Balan, D. R. Neuville, P. Trocellier, E. Fritsch, J.-P. Muller, G. Calas, *Am. Mineral.* **2001**, *86*, 1025.

[10] a) L. T. Silver, S. Deutsch, *J. Geol.* **1963**, *71*, 721; b) L. Nasdala, R. T. Pidgeon, D. Wolf, G. Irmer, *Mineral. Petrol.* **1998**, *62*, 1; c) N. G. Rizvanova, O. A. Levchenkov, A. E. Belous, N. I. Bezmen, A. V. Maslenikov, A. N. Komarov, A. F. Makeev, L. K. Levskiy, *Contrib. Mineral. Petrol.* **2000**, *139*, 101; d) D. W. Davis, T. E. Krogh, *Chem. Geol.* **2000**, *172*, 41, e) R. Romer, *Contrib. Mineral. Petrol.* **2003**, *145*, 481.

[11] a) R. C. Ewing, *Can. Mineral.* **2001**, *39*, 697; b) G. R. Lumpkin, *Elements* **2006**, *2*, 365.

[12] a) W. C. Brøgger, *Geol. Fören. Stock. För.* **1881**, *5*, 326; b) W. C. Brøgger, 'Die Mineralien der südnorwegischen Granitpegmatitgänge. I. Niobate, Tantalate, Titanate und Titanoniobate', *Videnskabs-Selskrabets Skrifter., Math.-Naturv. Klasse, no. 6*, **1906**; c) H.-J. Berg, *Bergverksmuseet Skrift* **1999**, *15*, 15.

[13] a) N. H. Magnusson, *GGF* **1960**, *82*, 407; b) A. A. Polkanov, E. K. Gerling, *Ann. N.Y. Akad. Sci.* **1961**, *91*, 492; c) G. Vidal, M. Moczydłowska, *Precambrian Res.* **1995**, *73*, 197.

[14] J. T. Armstrong, *Microbeam Anal.* **1995**, *4*, 177.

[15] For more experimental details see L. M. Keller, R. Wirth, D. Rhede, K. Kunze, R. Abart, *J. Metamorph. Geol.* **2008**, *26*, 99.

[16] The SHRIMP II used in this study is operated by a consortium consisting of Curtin University of Technology, the University of Western Australia, and the Geological Survey of Western Australia.

[17] For more experimental details see a) J. R. De Laeter, A. K. Kennedy, *Int. J. Mass Spectrom.* **1998**, *178*, 43; b) G. Foster, P. Kinny, D. Vance, C. Prince, N. Harris, *Earth Planet. Sc. Lett.* **2000**, *181*, 327.

[18] P. Kinny, 'Users guide to U–Th–Pb dating of titanite, perovskite, monazite and baddeleyite using the W.A. SHRIMP', Curtin University of Technology, School of Physical Sciences, report SPS 693/1997/AP72, **1997**, available from the author.

[19] A.-M. Seydoux-Guillaume, R. Wirth, L. Nasdala, M. Gottschalk, J. M. Montel, W. Heinrich, *Phys. Chem. Mineral.* **2002**, *29*, 240.

[20] L. P. Black, J. D. Fitzgerald, S. L. Harley, *Contrib. Mineral. Petrol.* **1984**, *85*, 141.

[21] A. Meldrum, L. A. Boatner, W. J. Weber, R. C. Ewing, *Geochim. Cosmochim. Ac.* **1998**, *62*, 2509.

[22] L. Nasdala, M. Wildner, R. Wirth, N. Groschopf, D. C. Pal, A. Möller, *Mineral. Petrol.* **2006**, *86*, 1.

[23] A.-M. Seydoux-Guillaume, J.-M. Montel, R. Wirth, B. Moine, *Chem. Geol.* **2008**, *261*, 318.

[24] A.-M. Seydoux-Guillaume, P. Goncalves, R. Wirth, A. Deutsch, *Geology* **2003**, *31*, 973.

[25] J. M. Montel, S. Foret, M. Veschambre, C. Nicollet, A. Provost, *Chem. Geol.* **1996**, *131*, 37; *cf.* also A. Cocherie, F. Albarede, *Geochim. Cosmochim. Ac.* **2001**, *65*, 4509.

[26] F. Poitrasson, S. Chenery, D. J. Bland, *Earth Planet. Sc. Lett.* **1996**, *145*, 79.

[27] a) C. M. Pointer, J. R. Ashworth, R. A. Ixer, *Mineral. Petrol.* **1988**, *39*, 21, b) L. Nasdala, A. Kronz, R. Wirth, T. Váczi, C. Pérez-Soba, A. Willner, A. K. Kennedy, *Geochim. Cosmochim. Ac.* **2009**, *73*, 1637.

[28] a) H. D. Holland, D. Gottfried, *Acta Cryst.* **1955**, *8*, 291; b) T. Murakami, B. C. Chakoumakos, R. C. Ewing, G. R. Lumpkin, W. J. Weber, *Am. Mineral.* **1991**, *76*, 1510

[29] a) A. Lanzirotti, G. N. Hanson, *Contrib. Mineral. Petrol.* **1996**, *125*, 332; b) F. Finger, I. Broska, M. P. Roberts, A. Schermeier, *Am. Mineral.* **1998**, *83*, 248; c) I. Broska, C. T. Williams, M. Janák, G. Nagy, *Lithos* **2005**, *82*, 71; d) J. Majka, B. Budzyń, *Mineralogia Polonica* **2006**, *37*, 61.

[30] D. E. Harlov, H.-J. Förster, T. G. Nijland, *Am. Mineral.* **2002**, *87*, 245.

[31] D. E. Harlov, R. Wirth, H.-J. Förster, *Contrib. Mineral. Petrol.* **2005**, *150*, 268.

[32] A.-M. Seydoux-Guillaume, R. Wirth, J. Ingrin, *Eur. J. Mineral.* **2007**, *19*, 7.

[33] C. J. Hetherington, D. E. Harlov, *Am. Mineral.* **2008**, *93*, 806.

[34] a) L. Hecht, M. Cuney, *Miner. Deposita* **2000**, *35*, 791; b) R. Mathieu, L. Zetterström, M. Cuney, F. Gauthier-Lafaye, H. Hikada, *Chem. Geol.* **2001**, *171*, 147; c) M. Stanisławska, M. Michalik, *Min. Soc. Poland – Special Papers* **2003**, *23*, 160; d) D. Papoulis, P. Tsolis-Katagas, C. Katagas, *Appl. Clay Sci.* **2004**, *24*, 271; e) R. Grapes, K. Bucher, P. W. O. Hoskin, *Eur. J. Mineral.* **2005**, *17*, 553; f) B. Rasmussen, J. R. Muhling, *Chem. Geol.* **2009**, *264*, 311.

[35] D. Read, M. A. G. Andreoli, M. Knoper, C. T. Williams, N. Jarvis, *Eur. J. Mineral.* **2002**, *14*, 487.

[36] Y. Pan, M. E. Fleet, *Mineral. Mag.* **1993**, *57*, 697.

[37] C. Doelter, H. Sirk, *Monatsh. Chem.* **1910**, *31*, 319.

[38] O. Kress, F. J. Metzger, *J. Am. Chem. Soc.* **1909**, *31*, 640.

[39] S. Teufel, C. A. Heinrich, *Chem. Geol.* **1997**, *137*, 273.

[40] A. Putnis, *Mineral. Mag.* **2002**, *66*, 689.